FERMILAB-PUB-19-113-TD
ACCEPTED

Measurements and Modelling of Mechanical Properties of Nb_3Sn Strands, Cables and Coils

E. Barzi, *Senior Member, IEEE,* C. Franceschelli, I. Novitski, F. Sartori, and A.V. Zlobin

***Abstract*—High field Nb_3Sn magnets for the next generation of hadron colliders are known to have long trainings and to be limited at 90% of their short sample limit at best. This means that the conductor current is at 60% or less of its critical value. Homogeneous finite element models are typically used for the complex system that includes coils, wedges, poles, yoke, rods, keys, shoes, fillers, shell, etc. Through both modeling and measurements of mechanical properties, we show how a more accurate sub-modelling of the composite structure allows for a better understanding of the stress and strain distributions. This is extremely important for Nb_3Sn performance since state-of-the-art high critical current wires of this superconductor are particularly sensitive to strain.**

***Index Terms*—Finite element analysis, Nb_3Sn technology, Rutherford cable, Sub-modelling, Superconducting accelerator magnet**

I. INTRODUCTION

THE Nb_3Sn accelerator magnet technology remains a challenging one after decades of research and development. However, it will be needed to achieve a nominal operation field of at least 15 to 16 T required in Hadron Colliders with energy reach beyond the LHC [1]-[3]. Envisioned for these future machines, in addition to the high field dipoles to bend the particle beam in the collider ring, are high-gradient quadrupoles, to collimate the beam in the transverse plane, and sextupoles to correct the trajectory.

The U.S. Magnet Development Program (MDP) [4] is developing a single-aperture 15 T Nb_3Sn dipole demonstrator [5] as a first step towards 16 T dipole magnets. It is based on a 4-layer graded cos-theta coil with 60 mm aperture and cold iron yoke. In a cos-theta dipole, due to Lorentz forces during operation, the coils ovalize along the mid-plane, i.e. the horizontal symmetry plane. The Lorentz force can be decomposed in two components, one radial and one azimuthal. The mechanical structure is therefore designed to provide pre-compression along the vertical plane of symmetry to prevent any detachment of the coil from the pole.

Coils are wound out of insulated Rutherford cables, made of dozens of strands compacted in a keystone structure, with a central stainless steel tape [6]-[9]: an example of Rutherford cable cross section is shown in Fig. 3 (bottom). After high temperature reaction in vacuum or inert atmosphere, coils are impregnated with epoxy.

The MDP is presently using Internal Tin Nb_3Sn of the Restacked Rod Process (RRP) kind [10]. The RRP is based on assembling a large number of Nb filaments and pure Sn or Sn-alloy rods in a Cu matrix. Each assembly is surrounded by a Nb barrier to prevent Sn diffusion into the high-purity Cu matrix, and it is then cold-drawn down to final size. Figure 1 shows the cross section of an RRP wire with 150 superconducting hexagonal subelements over a total of 169 restacks before reaction. After reaction, each hexagonal area occupied by the Nb filaments becomes a coalesced Nb_3Sn region, and each Sn core becomes bronze.

During its life cycle, the Nb-Sn composite first and the Nb_3Sn next, i.e. after heat treatment, are subject to several loads in the following sequential steps:

- Wire manufacturing: imparts drawing stress to the Nb, Sn and Cu components;
- Cable manufacturing: imparts plastic deformations on the Nb, Sn and Cu components;
- Coil heat treatment: after formation of the Nb_3Sn, the latter is compressed due to differential thermal contraction with respect to the Cu;
- Magnet assembly: pre-compressive stress is provided along the vertical plane through interference or other methods, to contrast the Lorentz force pressure along the mid-plane;
- Magnet cool-down from room temperature to 4.2 K or other cryogenic temperature: generates new stress state due to differential thermal contraction among parts;

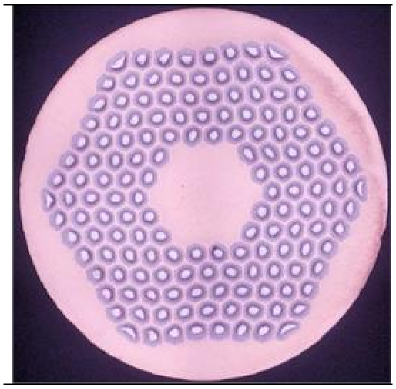

Fig. 1. Cross section of Nb_3Sn wire of the Restacked Rod Process type [10].

Manuscript receipt and acceptance dates will be inserted here. Work supported by U.S. DOE contract No. DE-AC02-07CH11359 in the context of broader collaboration with the US Magnet Development Program.

All authors are with the Fermi National Accelerator Laboratory, Batavia, IL 60510, USA (e-mail: barzi@fnal.gov). C. Franceschelli and F. Sartori are also with the University of Pisa, Italy.

Color versions of one or more of the figures in this paper are available online at http://ieeexplore.ieee.org.

Digital Object Identifier will be inserted here upon acceptance.

This manuscript has been authored by Fermi Research Alliance, LLC under Contract No. DE-AC02-07CH11359 with the U.S. Department of Energy, Office of Science, Office of High Energy Physics.

- Magnet operation: Lorentz forces add to the stress state.

Failure modes in Nb_3Sn coils include excessive stress or strain on the conductor, and detachment between coil components.

II. SUB-MODELLING OF 10-STACK TEST AT 300 K

A. *Premise*

Homogeneous finite element models are typically used for the complex system that includes coils, wedges, poles, yoke, rods, keys, shoes, fillers, shell, etc. The results of homogenous models are the average stress and strain values that are useful in the design of the mechanical structure. However, these models do not provide information on local stress and strain states in the coils. An alternative method called sub-modelling combines Finite Element Techniques with the theory of composite materials, and specifically the mechanical theory of a laminated section. This theory is based on the Kirchhoff-Love hypothesis and rigid interface between two layers. These two hypotheses are met in the modeling of a 10-stack test, i.e. ten insulated Rutherford cable samples stacked on top of each other and vacuum impregnated before compression testing in three directions [11]-[13]. Figure 2 shows a 10-stack sample (left), and the fixed and movable jaws used to apply compression (right).

B. *Macro and Meso Mechanical Models*

As homogeneous model for this study, we chose the simplest kind, i.e. the orthotropic transversally isotropic model, which represents a *macro mechanical model* of a homogenous material with anisotropic properties. The compliance matrix is composed as follows:

$$C = \begin{bmatrix} \frac{1}{E_\perp} & -\frac{\nu_\perp}{E_\perp} & -\frac{\nu_{13}}{E_\parallel} & 0 & 0 & 0 \\ -\frac{\nu_\perp}{E_\perp} & \frac{1}{E_\perp} & -\frac{\nu_{13}}{E_\parallel} & 0 & 0 & 0 \\ -\frac{\nu_{13}}{E_\parallel} & -\frac{\nu_{13}}{E_\parallel} & \frac{1}{E_\parallel} & 0 & 0 & 0 \\ 0 & 0 & 0 & \frac{1}{2G_{13}} & 0 & 0 \\ 0 & 0 & 0 & 0 & \frac{1}{2G_{13}} & 0 \\ 0 & 0 & 0 & 0 & 0 & \frac{1}{2G_{12}} \end{bmatrix} \quad (1),$$

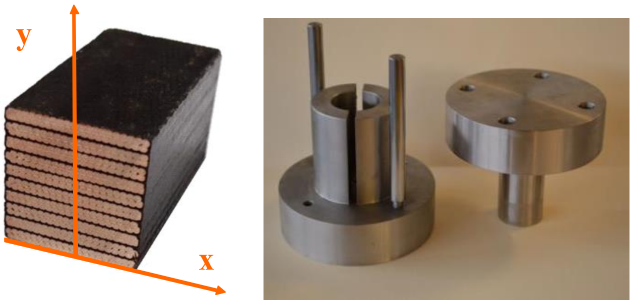

Fig. 2. 10-stack picture (left), and movable and fixed jaws (right) [11]-[13].

where:

$$E_\perp = E_1 = E_2,$$

$$E_\parallel = E_3,$$

$$\nu_\perp = \nu_{12} = \nu_{21},$$

$$G_{13} = G_{23}, \text{ and}$$

$$G_\perp = G_{12} = E_\perp/[2\,(1+\nu_\perp)] \qquad (2).$$

E_i are the Young moduli, G_{ij} are the shear moduli, and ν_{ij} are the Poisson ratios.

In the *meso mechanical model* that was used for this study, the composite elementary cell is comprised of a homogenous strand, or fiber, with epoxy and insulation. Figure 3 shows an example of a Rutherford cable (top) and such meso mechanical model in a Rutherford cable (bottom). For elements stressed parallel to the strands, deformation of the composite components at the interface must be the same for congruence. Therefore:

$$E_\parallel = v_f E_f + v_m E_m \text{ and}$$

$$\nu_{13} = \nu_{23} = v_f \nu_f + v_m \nu_m \text{ (direct law of mixtures),}$$

where E_f and E_m are the Young moduli of wire and epoxy/insulation respectively, and v_f and v_m are their volume fractions in the composite. For elements stressed perpendicularly to the strand direction:

$$1/E_\perp = v_f/E_f + v_m/E_m \text{ and}$$

$$1/G_{13} = 1/G_{23} = v_f/G_f + v_m/G_m \text{ (inverse law of mixtures),}$$

where G_f and G_m are the shear moduli of wire and epoxy/insulation respectively.

C. *Measurement of Mechanical Properties*

To verify some of the property values typically found in literature and for use in the models, unreacted Nb-Sn, cold-worked Cu, reacted Nb_3Sn and annealed Cu wires were measured with an Instron machine at room temperature. Figure 4 shows examples of tensile test results for an unreacted Nb-Sn composite wire (top), and for a reacted Nb_3Sn multifilamentary wire (bottom). Over 15 samples tested, the average ultimate stress for the former was 630 MPa ± 5%, and over 11 samples tested, the Young modulus for the latter was 53 GPa ± 10%.

D. *Finite Element Analysis of Whole 10-Stack*

The following was the very first modelling phase that was performed in this study. To understand first-order effects of stress distribution in a composite vs. homogenous material, five models of 10-stack half-samples were created with increasing

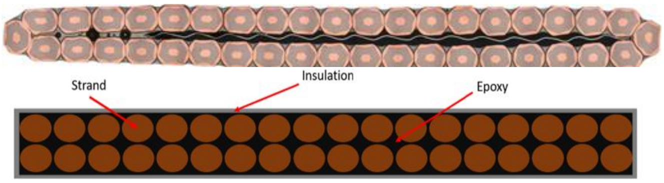

Fig. 3. Cross section of Rutherford cable (top), and meso mechanical model for Rutherford cable (bottom).

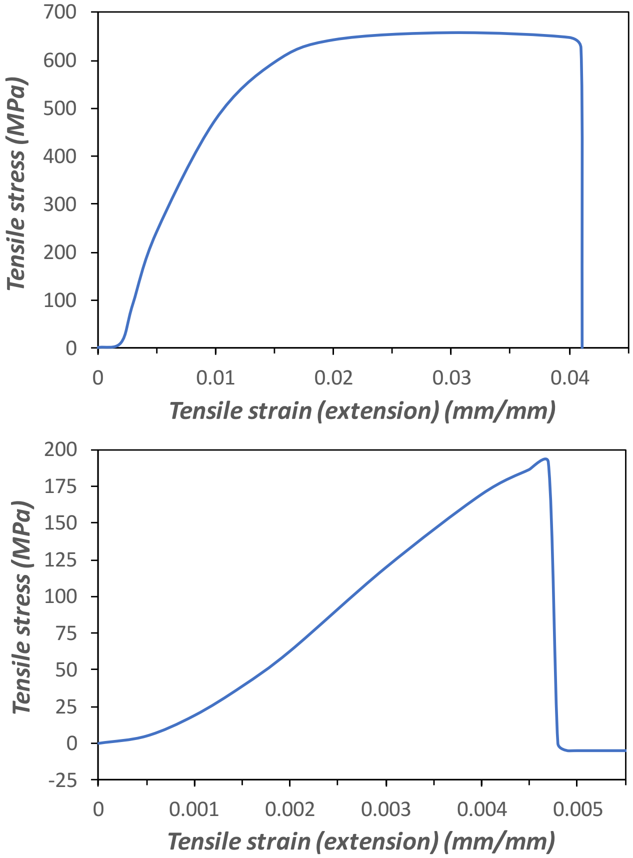

Fig. 4. Example of tensile test results for unreacted Nb-Sn composite wire (top), and for reacted Nb_3Sn multifilamentary wire (bottom).

level of detail using ANSYS in APDL mode. *Model 1* had 10 homogeneous layers with anisotropic properties and a Young modulus of 44 GPa; *Model 2* had 9 homogeneous layers as above, and one modelled with elementary cells; *Model 3* had 9 homogeneous layers and one modelled with more detailed cells, where the hexagonal Nb_3Sn region is separated from the Cu internal and outer areas: an example of these more detailed cells in a Rutherford cable is shown in Fig. 6 (bottom); *Model 4* had all 10 layers modelled with the elementary cell; and *Model 5* had all 10 layers modelled with the more detailed cells (see Fig. 5).

At first *Models 2* to *5* were loaded with a ramped uniform pressure on the upper boundary, up to 40 MPa, 80 MPa and 120 MPa of maximum pressure. To represent the contact with the fixed jaw, vertical displacements of the lower face were set to zero. To represent the structure symmetry, horizontal displacements of the left boundary, or axis of symmetry, were set to zero. Nb_3Sn, insulation and epoxy were modelled as linear elastic materials, whereas for the Cu and the homogenous strand an elastic perfectly plastic behavior was used.

All model components were created through element PLANE182, with the *generalized* plane strain option activated, to represent free transverse deformation during the compressive test. The plane strain assumption is typically used in modelling of pressure transverse to cables [14]. Activating in addition the *generalized* choice, allows to have a homogeneous non-zero strain in the axial direction. The mesh included less than 10% of triangular elements to minimize dependency on mesh size. The AGLUE command was used to connect elements through a linear contact, in order to prevent detachment in this study.

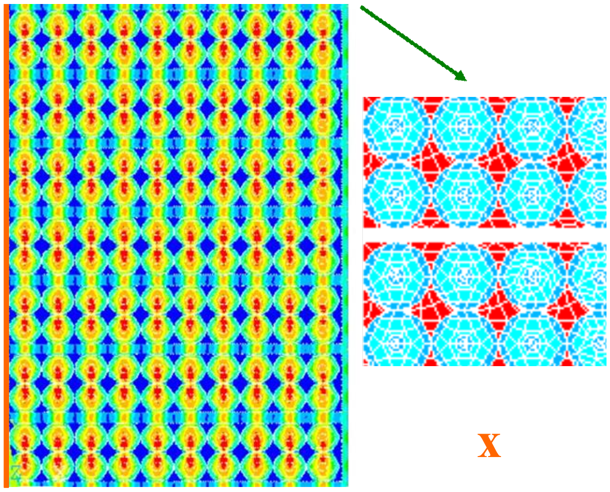

ap-

To study relative effects of stress distribution vs. homogenous conditions, the five models were kept simple, for instance no residual stresses were included, no stainless steel core was present, upper and lower strands in a cable are in point contact through a thin layer of epoxy, no work hardening is introduced.

Figure 5 indicates that the critical zones in cables are located in the contact regions between upper and lower strands. The models were compared for Von Mises equivalent stress, Von Mises equivalent strain, displacement along x and displacement along y. Table I shows the maximum values obtained for the Von Mises equivalent stress, and the y displacement of the upper face for the three loads applied. The local stress enhancement factor k with respect to the applied pressure σ_{ext_av}, defined as:

$$k = \sigma_{int\_max} / \sigma_{ext\_av},$$

is greater than 2 for all models. *Models 4* and *5* provided very similar values for the compared parameters. The difference in the maximum Von Mises stress between *Models 4* and *5* was ~5% only, and the two models had identical y displacements. The variation in the maximum Von Mises stress among the 10 cables in the modelled 10-stack was less than 1% for *Model 4* and less than 3% for *Model 5*. At 80 MPa of applied pressure, the maximum Von Mises equivalent strain was 0.0333 with a variation of less than 2% in *Model 4* and 0.0347 with a ~4%

TABLE I
MODELS COMPARISON

Model No.	Von Mises max. equiv. stress, MPa			Upper face *Y* displacement, mm		
	40 MPa	80 MPa	120 MPa	40 MPa	80 MPa	120 MPa
2	90	180	260	-0.016	-0.031	-0.046
3	95	190	285	-0.015	-0.030	-0.045
4	84	167	250	-0.022	-0.045	-0.067
5	87	174	260	-0.022	-0.045	-0.067

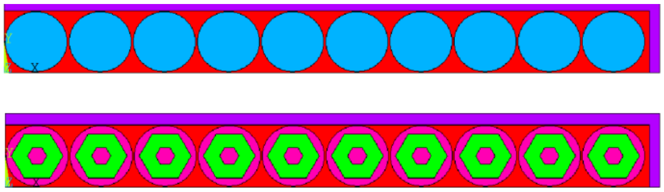

Fig. 6. Finite element models for a quarter of a Rutherford cable with elementary cell (top) and more detailed cell (bottom).

variation in *Model 5*. When analyzing the maximum Von Mises stress distribution in strands along a central cable (the 5th cable from the bottom) in the 10-stack sample, it varied within only 2% in *Model 4* and within 4% in *Model 5*.

The models were also run with a load applied in the x direction, with similar results in the distribution and factor enhancement of local Von Mises stress.

E. Simplified Finite Element Analysis

Next, a quarter of a cable was modeled with the same material properties and model hypotheses, and again by using both the elementary cell and the more detailed one, as shown in Fig. 6. The model was run also on a single elementary cell, i.e. as if extracted from the cable, with the added constraint of plane conservation for the right boundary, i.e. same x displacement for points belonging to boundary face. The maximum Von Mises stress and strain values are shown in Table II for the three aforementioned models. In Figure 7 the Von Mises stress distribution between the complete 10-stack *Models 4* and *5* are also compared with the results obtained for the single elementary cell. As can be seen, the results of the single elementary cell model are in excellent consistency with those of the more complex models. The single elementary cell was therefore used for a sensitivity analysis of the model to several parameters and to characterize the orthotropic transversally isotropic behavior of a homogenous coil package.

F. Characterization of Composite as Homogeneous Material

To characterize the compliance matrix (1) of a composite as an orthotropic transversally isotropic homogenous material, the elementary cell model was used, but instead of applying a constant pressure, known displacements were imposed as loads.

TABLE II
SIMPLIFIED MODELS COMPARISON

Model	Von Mises max. equiv. stress, MPa			Von Mises max. equiv. strain		
	40 MPa	80 MPa	120 MPa	40 MPa	80 MPa	120 MPa
Cable/4 w/elementary cell	81.4	163	245	0.0177	0.0354	0.0531
Cable/4 w/detailed cell	82.6	165	249	0.0178	0.0356	0.0535
Elementary cell	81.6	163	245	0.0170	0.0340	0.0511

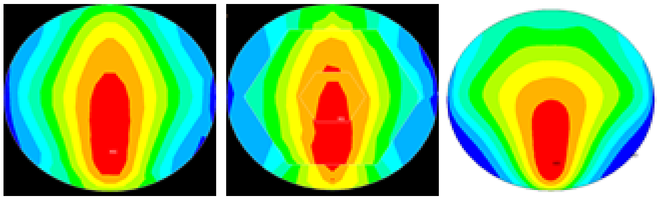

Fig. 7. Von Mises stress distribution in strand from *Model 4* (left), *Model 5* (center) and in single elementary cell model (right).

To determine Young modulus $E_\perp = \sigma_{av}/\ \varepsilon_y$, a y displacement is applied on the upper surface. The upper contour reaction forces are then integrated along the direction perpendicular to the loading with the FSUM command, and the average stress σ_{av} obtained by dividing the integrated value by the width of the cell. This process is repeated at increasing y displacement values to obtain the stress-strain characteristic, as shown in Fig. 8. To determine Poisson ratio $\nu_\perp = -\varepsilon_x/\ \varepsilon_y$, the x displacement of the free face is obtained from the model. Shear modulus $G_\perp$ is then determined from (2). The following values were obtained:

$$E_\perp = 29 \text{ GPa};$$

$$\nu_\perp = 0.26;$$

$$G_\perp = 11.5 \text{ GPa}.$$

The above procedure can be repeated by applying x displacements. The following values were obtained:

$$E_\perp = 30.5 \text{ GPa};$$

$$\nu_\perp = 0.27;$$

$$G_\perp = 12 \text{ GPa}.$$

The consistency between the two sets of values shows the solidity of the model. When repeating the procedure with *Model 4* and the quarter of a cable model with the elementary cell, $E_\perp$ was 29.5 GPa and 28.5 GPa respectively.

To determine Young modulus E_z, shear moduli G_{xz} and G_{yz}, Poisson ratios ν_{xz} and ν_{yz}, the previously described laws of mixtures can be used.

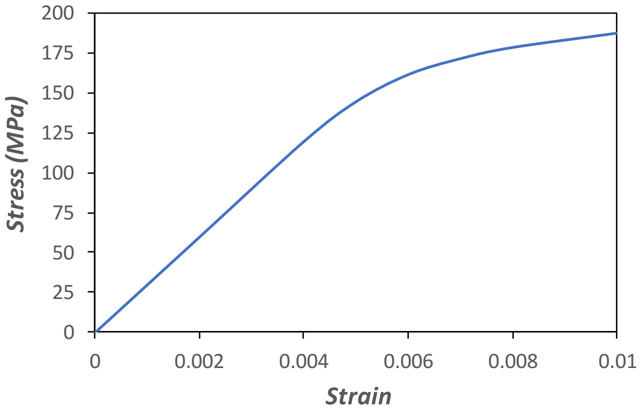

Fig. 8. Example of stress-strain characteristic (compression along y axis) obtained from the elementary cell model for a composite as homogeneous material.

G. *Sensitivity Analysis*

Sensitivity of the elementary cell model to material and geometrical properties was studied extensively by varying one at a time Young modulus of epoxy, Young modulus of insulation, Young modulus of the strand, amount of epoxy between strand layers in cables, shape of the strands, presence of stainless steel core in cables, etc. Some relevant results are shown in Fig. 10. One can see from Fig. 9, top, that the local stress enhancement factor k decreases by increasing the Young modulus, or stiffness, of the epoxy. These results are remarkably consistent with [14]. Also, the Young modulus of the equivalent homogeneous material obtained with the procedure described in II.F increases with both the epoxy (Fig. 10, center) and wire (Fig. 10, bottom) rigidities, as expected.

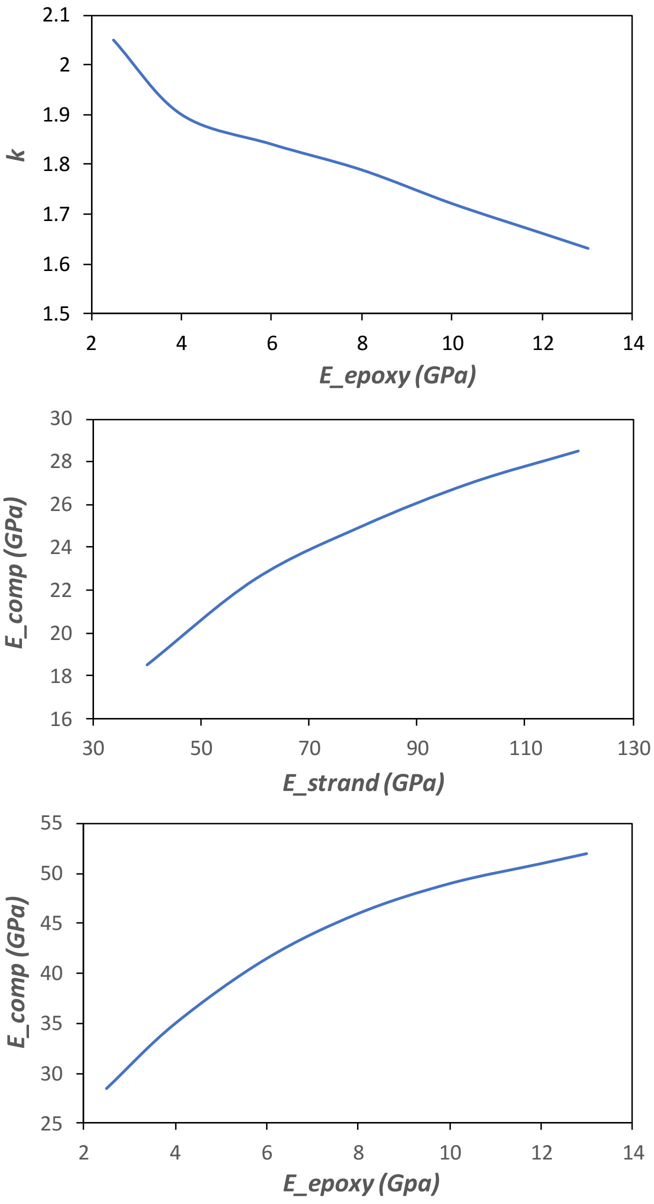

Fig. 9. Sensitivity of local stress enhancement factor k to epoxy Young modulus (top), sensitivity of composite Young modulus to epoxy Young modulus (center), and to strand Young modulus (bottom).

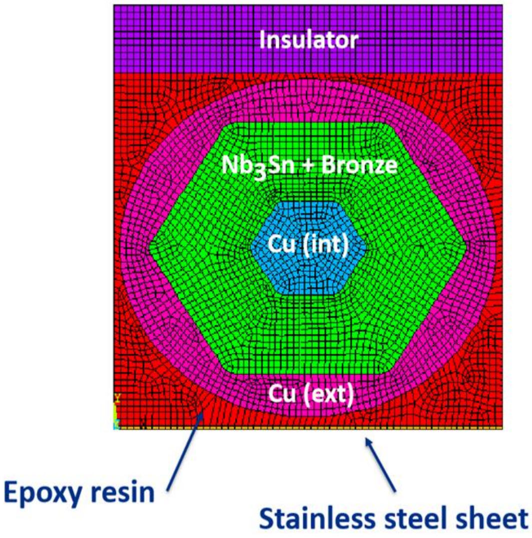

Fig. 10. Detailed cell used for 10-stack modelling at 4.2 K.

III. SUB-MODELLING OF 10-STACK TEST AT 4.2 K

A. *Premise*

The simplified single cell concept works in place of modelling the whole 10-stack geometry thanks to the high level of symmetry of the problem. Clearly, not all geometrical features are represented, for instance irregularities in the geometry of the cable, presence of a keystone angle, variation in the relative position of the strands in the cable, etc. However, having been proven useful in providing stress and stiffness of the coil composite, the concept was applied to a more detailed cell to improve the level of accuracy in the analysis when cooling the system down to 4.2 K. The schematic of this more detailed cell is shown in Fig. 10. The inner and outer Cu regions are treated each with its own material properties to study the effect of stronger Cu alloy materials in the wire. The non-Cu part is treated as a homogeneous mixture of Nb_3Sn and of residual bronze from the heat treatment. The same PLANE182 elements with the generalized strain option were used, and with isotropic and bi-linear material properties for the composite components. Boundary conditions included planarity of both the upper and the right surfaces of the cell. The properties used for all materials in the composite are shown in Table III, where s_y is the yield strength, and α is the coefficient of thermal expansion.

TABLE III
MATERIALS PROPERTIES

Materials	E, GPa	s_y, MPa	ν	α, 10^{-6}/ K
Epoxy resin (CTD 101K)	2.4	150	0.4	50
Insulator (S-2 Glass + CTD 101K)	19	320	0.3	36
Stainless steel	206	800	0.3	12
Nb_3Sn	125	800	0.37	7
OHFC Cu (annealed)	118	100	0.36	17
GlidCop	118	450	0.36	17
Bronze	118	110	0.36	17

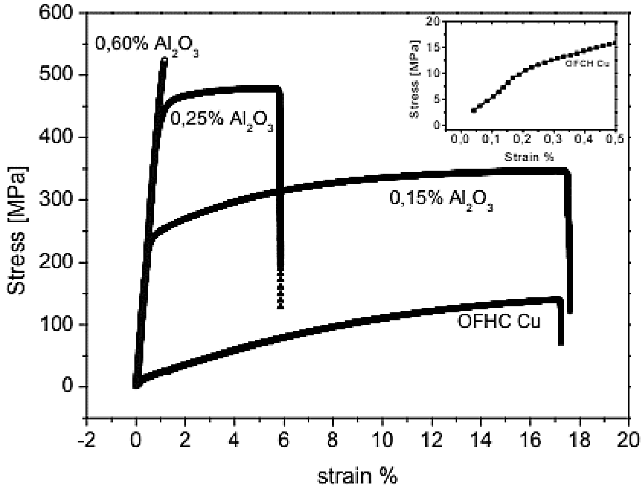

Fig. 11. GlidCop properties as found in literature [15].

B. *Modelling of Compression Test at 300 K*

The load was applied as a uniform displacement of the upper surface, up to 80 MPa of average external pressure. No residual strains were considered from the heat treatment process. A sensitivity analysis to Cu yield strength in the inner and outer Cu regions was performed. Cu is a linearly hardening plastic material, whose properties are uncertain after the high temperature heat treatment required to produce Nb_3Sn. GlidCop Al-15 has a higher yield strength after heat treatment, but also has a larger electrical resistivity than Cu. Figure 11 compares stress and strain characteristics of OFHC Cu with some GlidCop alloys as found in literature [15]. In the model the Cu was replaced with GlidCop in either Cu region or in both to gauge the effects on stress and strain distributions. Figure 12 shows the results of this study. At room temperature, the largest reduction on the local stress enhancement factor *k* is for the GlidCop to be in the central area of the wire. Distributions of the equivalent Von Mises stress are shown in Fig. 13 for the maximum applied external pressure of 80 MPa, and for different combinations of

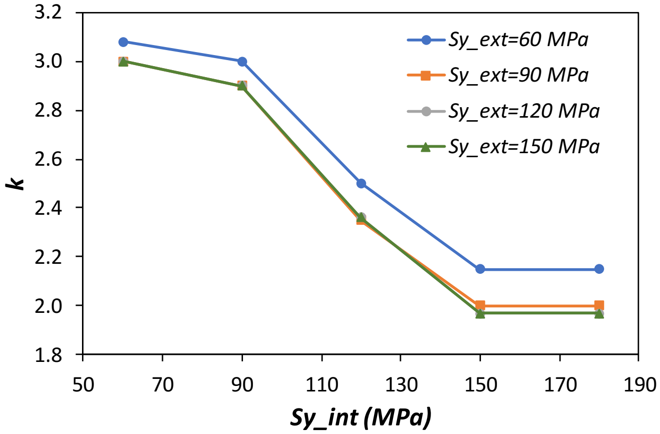

Fig. 12. Sensitivity at room temperature of local stress enhancement factor *k* to yield strength s_{Yint} of the inner Cu region, represented on the horizontal axis, and to yield strength s_{Yext} of the outer Cu region, represented in legend.

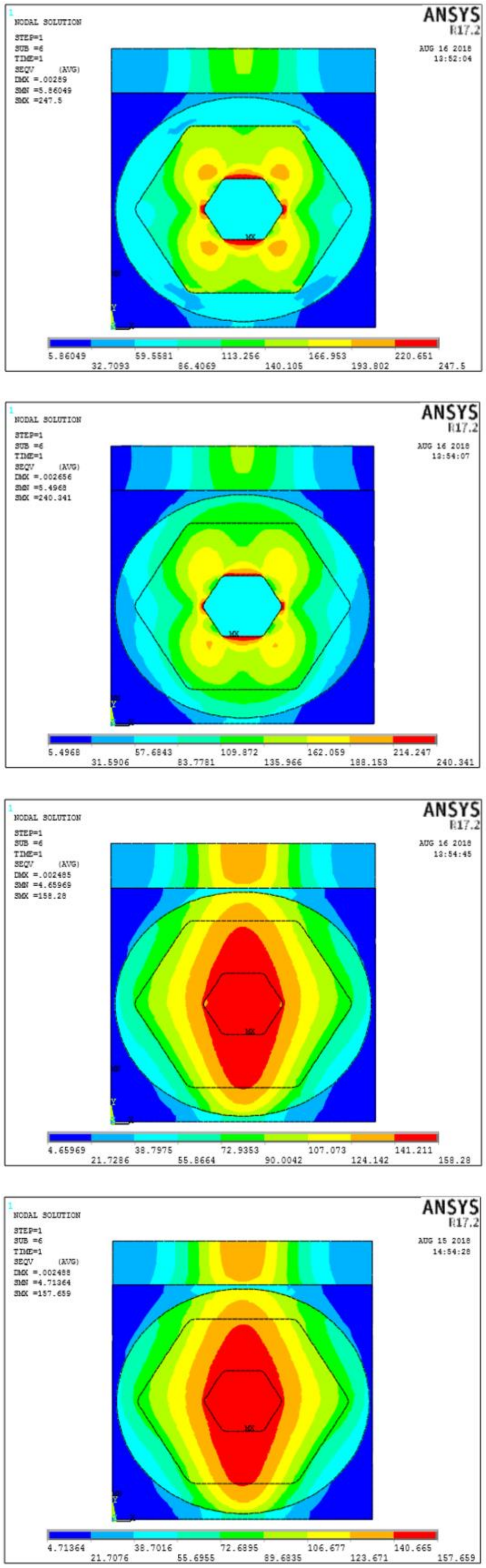

Fig. 13. Equivalent Von Mises stress distributions at room temperature for an applied external pressure of 80 MPa, and for different combinations of yield strengths in the inner and outer Cu regions of the strand. Top represents s_{Yint} = 60 MPa and s_{Yext} = 60 MPa, second from the top s_{Yint} = 60 MPa and s_{Yext} = 180 MPa, third s_{Yint} = 180 MPa and s_{Yext} = 60 MPa, and last s_{Yint} = 180 MPa and s_{Yext} = 180 MPa.

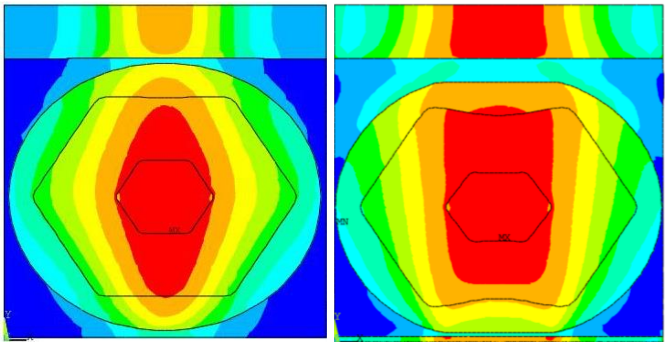

Fig. 14. Comparison on Von Mises stress distributions at room temperature in undeformed (left) and deformed (right) strand.

yield strengths in the inner and outer Cu regions of the strand. Here it is even more apparent how reinforcing the inner core of the wire redistributes and reduces, at room temperature, the localized peak stresses found on the innermost part of the superconducting hexagonal area into a larger region. This latter region resembles a vertical ellipse and encompasses the whole GlidCop wire core and most of superconducting hexagon width. By replacing Cu with GlidCop in the inner Cu regions of the Nb_3Sn wire, the maximum equivalent Von Mises stress at room temperature in the wire is reduced by 40%.

A sensitivity study to the size of the Nb_3Sn+bronze area was also performed. By increasing the outer hexagon radius by 50%, the local stress enhancement factor k decreases by only 1%. Thinning the hexagon by a factor of three reduces k by 0.1%.

Furthermore, the effect of an originally deformed shape for a strand in the cable was considered. The strand was deformed plastically through non-linear 2D contact analysis. A refined remesh was used on the deformed shape and the structural analysis performed by applying an external pressure. Figure 14 shows that the Von Mises stress distribution changes only slightly with respect to the undeformed strand.

C. *Modelling of Compression Test at 4.2 K*

Two cases were modelled. One where the load was first applied and then the sample cooled down from 300 K to 4.2 K, and another where the sample was first cooled down and then the load was applied. Since the difference in results between these two cases was minimal, we will refer to the latter in the following. The material properties used were the same as in Table III. The load was applied as uniform displacement of the upper surface, up to 80 MPa of average external pressure. A sensitivity analysis to Cu yield strength in the inner and outer Cu regions was performed also in this case. Distributions of the equivalent Von Mises stress are shown in Fig. 15 for the maximum applied external pressure of 80 MPa, and for different combinations of yield strengths in the inner and outer Cu regions of the strand. It can be seen how reinforcing the outer core of the wire redistributes and reduces, at helium temperature, the peak stresses localized on the outermost parts of the superconducting hexagonal area. By replacing Cu with GlidCop in the outer Cu regions of the Nb_3Sn wire, the maximum equivalent

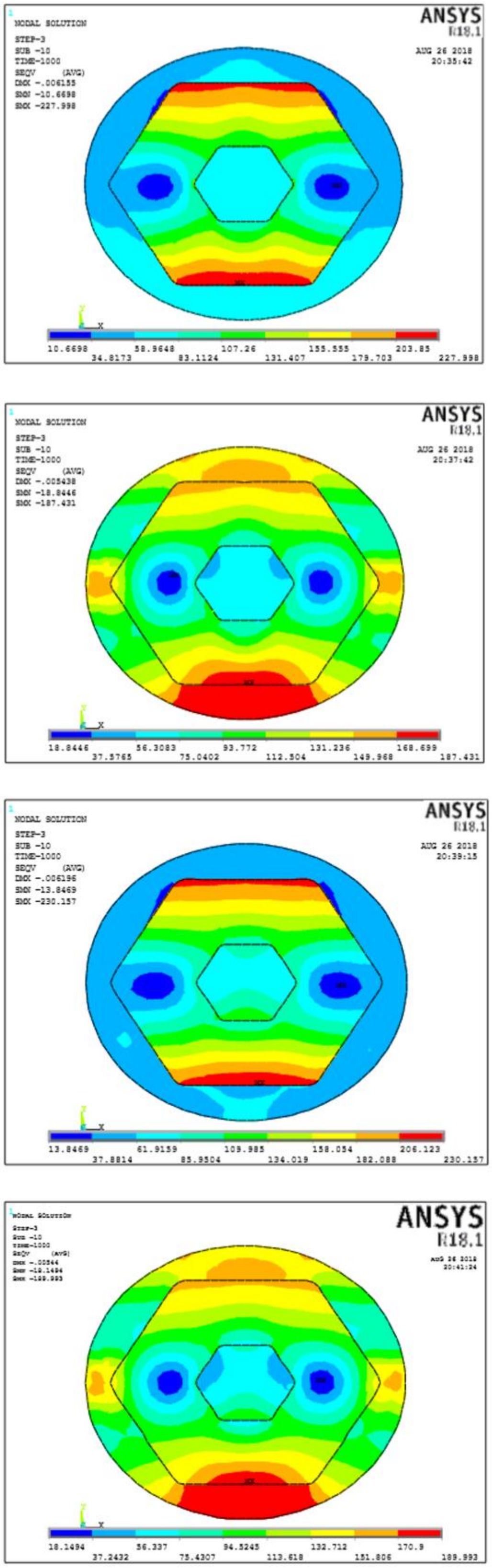

Fig. 15. Equivalent Von Mises stress distributions at 4.2 K for an applied external pressure of 80 MPa, and for different combinations of yield strengths in the inner and outer Cu regions of the strand. Top represents s_{Yint} = 60 MPa and s_{Yext} = 60 MPa, second from the top s_{Yint} = 60 MPa and s_{Yext} = 180 MPa, third s_{Yint} = 180 MPa and s_{Yext} = 60 MPa, and last s_{Yint} = 180 MPa and s_{Yext} = 180 MPa.

Von Mises stress at helium temperature in the wire is reduced by just less than 20% in the contact regions between upper and lower strands, but by more than 25% in the top outermost part of the superconducting hexagonal region, previously a critical area.

The sensitivity analysis showed a positive linear correlation between elastic moduli of epoxy, insulator and Nb_3Sn and the maximum stress in the Nb_3Sn area. However, the model is sensitive also to thermal expansion coefficients.

IV. CONCLUSION

Sub-modelling has been successfully used in the past to model plastic deformation in Nb-Sn composite wires. Comparisons with strand and cable data allowed the establishment of a failure criterion, i.e. equivalent plastic strain in the Cu component greater than 0.48 ± 0.1 [16]. This is useful for Rutherford cable design and fabrication and, in general, for Nb_3Sn pre-heat treatment mechanics. Identifying a similar criterion or set of criteria for post-processed superconducting Nb_3Sn wires would immensely help high field magnet designers.

In this paper sub-modelling was applied to a 10-stack test, where a stack of impregnated Rutherford cables is compressed along the x, y and z directions, one at a time, both at room temperature and at 4.2 K, to obtain the mechanical properties of the composite sample. Sub-modelling also allows to study stress and strain distributions in the sample and to identify critical areas of maximum equivalent Von Mises stress and strain.

It was shown that the behavior of the whole 10-stack sample is well represented by a single cell model, thanks to the symmetries of the problem. An elementary cell model first, and a more detailed cell model next, were used to study sensitivity of the model to various parameters both at room temperature and at 4.2 K.

Using this latter more detailed cell model, it was found that by replacing Cu with a stronger Cu, or GlidCop, in both the inner and outer Cu regions of Nb_3Sn wire, the maximum equivalent Von Mises stress in the wire was reduced by 40% at room temperature and by 20-25% at 4.2 K.

Experiments and detailed modelling used together will help understand which superconducting components among wire, cable and coils, are the most cost-effective to reinforce mechanically.

REFERENCES

[1] "Building for Discovery: Strategic Plan for U.S. Particle Physics in the Glocal Context," P5 Report, http://science.energy.gov/~/media/hep/hepap/pdf/May%202014/FINAL_P5_Report_053014.pdf

[2] CEPC/SppC study in China, http://indico.cern.ch/event/282344/session/1/contribution/65/material/slides/1.pdf

[3] D. Tommasini *et al*. "The 16 T dipole development program for FCC," *IEEE Trans. Appl. Supercond*., vol. 27, no. 4, Jun. 2017, Art. No. 4000405.

[4] The U.S. Magnet Deveopment Program Plan. Available online: https://science.energy.gov.

[5] I. Novitski *et al*., "Development of a 15 T Nb_3Sn Accelerator Dipole Demonstrator at Fermilab," *IEEE Trans. Appl. Supercond*., vol. 26, no. 4, Jun. 2016, Art. No. 4001007.

[6] G. Gallagher-Daggit, "Superconductor cables for pulsed dipole magnets," Technical report (Rutherford Laboratory Memorandum, No. RHEL/M/A25, 1973.

[7] J.D. Adam et al., "Rutherford Cables with Anisotropic Transverse Resistance", IEEE Trans. on Appl. Supercond., Vol. 7, No. 2, June 1997, p. 958.

[8] Andreev, N.; Barzi, E.; Borissov, E.; Elementi, L.; Kashikhin, V. S.; Lombardo, V.; Rusy, A.; Turrioni, D.; Yamada, R.; Zlobin, A. V., "Development of Rutherford-type Cables for High Field Accelerator Magnets at Fermilab", IEEE Transactions on Applied Superconductivity, Volume 17, Issue 2, June 2007 Page(s):1027-1030.

[9] R. M. Scanlan et al., "Fabrication of Rutherford-Type Superconducting Cables for Construction of Dipole Magnets," ICMC Conference, Shenyang, PR China, June 7-10, 1988.

[10] M. B. Field et al., "Optimizing conductors for high field applications," IEEE Trans. Appl. Supercond, vol. 24, no. 3, p. 6001105, Jun. 2014.

[11] D. Chichili D et al., "Investigation of Cable Insulation and Thermo-Mechanical Properties of Epoxy Impregnated Nb_3Sn Composite", IEEE Trans. Appl. Supercond. V. 10, No. 1, 2000, p. 1317.

[12] R. Bossert et al., "Tests of insulation systems for Nb_3Sn Wind and React Coils", AIP Conf. Proc. 986:161 2008.

[13] R. Bossert et al., "Recent Progress and Tests of Radiation Resistant Impregnation Materials for Nb_3Sn Coils", AIP Conf. Proc. 1574:132 2014.

[14] F. Wolf *et al*., "Characterization of the Stress Distribution on Nb_3Sn Rutherford Cables under Transverse Compression", *IEEE Trans. On Appl. Supercond*., vol. 28, no. 3, April 2018, Art. No. 8400106.

[15] A. Malagoli et al., "Study of the Superconducting and Thermal Properties of ex-situ GlidCop®-Sheathed Practical MgB_2 Conductors", *IEEE Trans. On Appl. Supercond*., vol. 19, no. 4, Aug. 2009, p. 3670.

[16] E. Barzi *et al*., "A Model to Study Plastic deformations in Nb_3Sn Wires," *IEEE Trans. Appl. Supercond.*, vol. 21, no. 3, p. 2588 (2011).